THE JOURNAL OF
PHYSICAL CHEMISTRY B

Article

pubs.acs.org/JPCB

Diameter-Dependent Bending Modulus of Individual Multiwall Boron Nitride Nanotubes

Adrienne E. Tanur,[†] Jiesheng Wang,[‡] Arava L. M. Reddy,[§,∥] Daniel N. Lamont,[§] Yoke Khin Yap,[‡] and Gilbert C. Walker*[,†,§]

[†]Department of Chemistry, University of Toronto, Toronto, Ontario M5S 3H6, Canada

[‡]Department of Physics, Michigan Technological University, Houghton, Michigan 49931-1295, United States

[§]Department of Chemistry, University of Pittsburgh, Pittsburgh, Pennsylvania 15260, United States

S *Supporting Information*

ABSTRACT: The mechanical properties of individual multiwall boron nitride nanotubes (MWBNNTs) synthesized by a growth-vapor-trapping chemical vapor deposition method are investigated by a three-point bending technique *via* atomic force microscopy. Multiple locations on suspended tubes are probed in order to determine the boundary conditions of the supported tube ends. The bending moduli (E_B) calculated for 20 tubes with diameters ranging from 18 to 58 nm confirm the exceptional mechanical properties of MWBNNTs, with an average E_B of 760 ± 30 GPa. For the first time, the bending moduli of MWBNNTs are observed to increase with decreasing diameter, ranging from 100 ± 20 GPa to as high as 1800 ± 300 GPa. This diameter dependence is evaluated by Timoshenko beam theory. The Young's modulus and shear modulus were determined to be 1800 ± 300 and 7 ± 1 GPa, respectively, for a trimmed data set of 16 tubes. The low shear modulus of MWBNNTs is the reason for the detected diameter-dependent bending modulus and is likely due to the presence of interwall shearing between the crystalline and faceted helical nanotube structures of MWBNNTs.

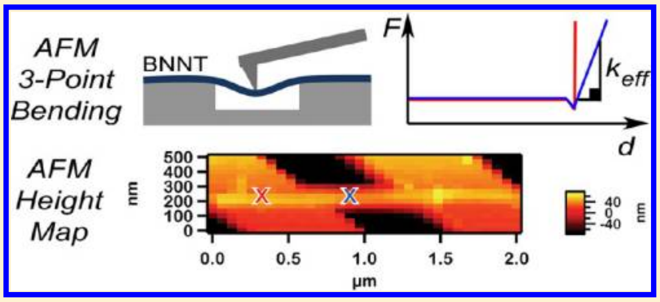

INTRODUCTION

Boron nitride nanotubes (BNNTs), first predicted in 1994[1,2] and synthesized in 1995,[3] have attracted increasing attention in recent years due to their unusual properties. Although structurally similar to carbon nanotubes (CNTs), BNNTs have significantly different optical and electronic properties. BNNTs are much more insulating than CNTs, with a band gap of 5−6 eV which is largely independent of tube chirality or diameter.[2] Theoretical studies have indicated that the axial Young's modulus of single wall BNNTs (SWBNNTs) is of the same order as that of carbon nanotubes (~1 TPa).[4,5] BNNTs' mechanical properties, together with their high aspect ratio, high thermal conductivity,[6] optical transparency, electrically insulating character, and high resistance to oxidation (up to 1100 °C),[7] make them ideal fillers for technologically relevant composite materials such as seals and encapsulants[8−11] and biomaterials.[12] In addition, BNNTs show promise for a diverse range of other applications, including hydrogen storage,[13,14] targeted drug delivery,[15] and optoelectronic devices such as lasers and light emitting diodes.[16,17]

For BNNTs to be successfully employed in the aforementioned applications, a better understanding of their mechanical properties is required. This is particularly important for applications which rely on the mechanical properties of individual tubes, such as resonators and sensors,[18] and microtubule mimics.[19] In contrast to CNTs, only a handful of experimental studies have been conducted on BNNTs to determine their Young's modulus. Chopra and Zettl[20] used the resonance technique of Treacy et al.[21] to determine that an arc-discharge multiwall BNNT (MWBNNT) (3.5 nm outer diameter) had a modulus of ~1.22 TPa. Electric-field-induced resonance experiments by Suryavanshi et al.[22] yielded moduli of 505−1031 GPa for a set of 18 tubes, with outer diameters ranging from 34 to 94 nm. Golberg et al.[23] determined moduli of 0.5−0.6 TPa (40 and 100 nm outer diameter tubes) *via* in situ bending experiments using an atomic force microscope (AFM) setup within a transmission electron microscope (TEM). Using a similar setup, Ghassemi et al.[24] measured five MWBNNTs with outer diameters of 38−51 nm, and found that the average modulus was ~0.5 TPa. Depending on the choice of shell thickness, the Young's modulus of a 1.9 nm diameter SWBNNT was found to range from 0.87 to 1.11 TPa.[25] The wide range of moduli observed indicates a need for further study in order to elucidate the influence of factors such

Special Issue: Paul F. Barbara Memorial Issue

Received: September 6, 2012
Revised: December 8, 2012
Published: December 19, 2012

as the synthesis technique, nanotube structure, and morphology on the Young's modulus.

Three-point bending tests conducted with AFM have been used to characterize the modulus of a variety of high aspect ratio structures, including CNTs,[26−28] nanowires,[29,30] and electrospun polymers.[31] Typically, the nanotubes or wires are deposited onto a stiff substrate with a topographical pattern, such as polished porous Al_2O_3 membranes or Si gratings patterned with trenches. The tubes occasionally lie over pores or trenches, and the midpoint of the suspended portion is subjected to a downward force applied by the AFM tip. Force−displacement curves are obtained, and the bending modulus can be calculated directly from the slope of the force curve together with the geometrical parameters of the tube's diameter and suspended length. In most studies, the supported beam ends are assumed to have clamped boundary conditions due to the adhesion between the nanomaterial and the substrate. However, this assumption can be unfounded and can be a source of systematic error in the determination of the bending modulus. Other beam end boundary conditions include simply supported and mixed support in which one end is clamped and the other end is simply supported. Depending on the support conditions, the solution of the Euler−Bernoulli beam equation takes on different forms, yielding different expressions for the bending modulus. The appropriate boundary conditions for an individual tube can be determined if multiple locations along the length of the suspended tube are probed. This allows for a more accurate determination of the modulus value, as demonstrated by Shanmugham et al.,[32] Chen et al.,[33] Kluge et al.,[34] and Gangadean et al.[35]

In this study, we use AFM to measure the bending modulus E_B of MWBNNTs synthesized by a growth-vapor-trapping chemical vapor deposition (GVT-CVD) technique.[36] A force mapping technique is used in order to collect force curves from various locations along the length of the suspended tube. We show that for our sample the majority of tubes possess simply supported ends instead of clamped ends. On the basis of these boundary conditions, we calculate the bending moduli for tubes of various diameters, and we present a discussion about the diameter dependence that is observed.

■ EXPERIMENTAL METHODS

MWBNNTs were synthesized *via* the growth-vapor-trapping chemical vapor deposition technique previously described by Lee and co-workers.[36] The MWBNNTs were collected on Si substrates and sonicated in ethanol to form a MWBNNT suspension.

The MWBNNTs were characterized with scanning electron microscopy (SEM), low and high resolution transmission electron microscopy (TEM, HR-TEM), and Fourier transform infrared spectroscopy (FTIR). The morphology of the as-synthesized MWBNNTs was characterized with SEM (S-4700, Hitachi, Japan). For the TEM measurements, the MWBNNT suspension was dropped onto a holey carbon TEM grid and allowed to dry. Bright-field low resolution TEM images were acquired at 30 kV, 17.5 μA emission current (S-5200, Hitachi, Japan). Bright-field HR-TEM images were acquired at 200 kV, 39 μA emission current (HD-2000, Hitachi, Japan). FTIR spectra were taken using an attenuated total internal reflection (ATR) setup. The MWBNNT suspension was dropped onto a ZnSe ATR crystal and allowed to dry. For comparison purposes, hexagonal boron nitride (*h*-BN) nanoparticles (MK-hBN-N70, MK Impex Canada, Mississauga, Ontario) were also characterized by FTIR. Spectra were recorded on a FTIR spectrometer (Spectrum BX, Perkin-Elmer, Waltham, MA) at a resolution of 1 cm^{-1}.

For the AFM sample preparation, the MWBNNT suspension was dropped onto clean Si substrates patterned with trenches 400 nm wide and 200 nm deep (LightSmyth Technologies, Eugene OR) and was allowed to dry. AFM height images of the tubes on the patterned substrate were acquired in air under ambient conditions using AC (intermittent contact) mode (MFP-3D, Asylum Research, Santa Barbara CA). Si probes (NCH, Nano World, Neuchâtel Switzerland) with tip radii of ~20 nm were used. The optical lever sensitivity of the cantilevers was calibrated by acquiring force curves in contact mode on a clean Si substrate. The spring constant of each cantilever used was determined by the thermal method and found to range from 33 to 46 N/m.[37] A discussion of the applicability of the thermal method for high spring constant cantilevers is presented in the Supporting Information. AFM force maps (typically 2 μm × 0.5 μm with 32 × 16 points) were obtained of MWBNNTs spanning trenches. A force curve (applied force F versus tip−sample separation) was collected at each point on the map. The force curves corresponding to the points along the suspended portion of the tube (as determined from the height map and the force curves themselves) were analyzed to extract the effective tube stiffness, k_{eff}, by a linear fit to the slope of the force curve. A more detailed description of the force mapping method is given in the Supporting Information.

The suspended length L for a given tube was determined from the AFM height map as well as from higher-resolution AFM height images acquired in tapping mode. The lateral dimension of the pixels making up the force map was used to estimate the errors associated with the values of position (a, b) and suspended length. The tube diameter was determined by the height of the tube on the substrate from the tapping mode height images.

■ RESULTS AND DISCUSSION

Characterization of MWBNNTs. Electron microscopy images of the MWBNNTs produced by the GVT-CVD method are shown in Figure 1. The scanning electron microscope (SEM) image in Figure 1a shows straight fibers with diameters ranging from ~15 to 60 nm. Figure 1b depicts a low resolution bright field TEM image of the as-synthesized MWBNNTs, and confirms the hollow tubular nature of the fibers. A high resolution TEM image of a dark region in a tube wall is shown in Figure 1c. The layers appear crystalline with an interlayer spacing of ~0.34 nm, as determined from the (002) diffraction spots in the fast Fourier transform for this region (not shown). This spacing is consistent with the crystal structure of hexagonal boron nitride and BNNTs.[24,36]

The FTIR spectrum of the MWBNNTs is shown in Figure 2. For comparison, the spectrum for commercially available hexagonal BN (*h*-BN) nanoparticles is also given. The broadness of the *h*-BN peaks is likely due to due to both size distribution as well as defects within the crystal structure, predominantly on the edges of the nanoparticles. The MWBNNT spectrum exhibits peaks at ~1368 and ~1510 cm^{-1}, which correspond to the in-plane transverse optical (TO) and longitudinal optical (LO) E_{1u} modes of *h*-BN. The TO E_{1u} mode is a stretching mode along the tube axis, while the LO E_{1u} mode is a stretching mode along the tube circumference. A weak feature at around 800 cm^{-1} is shown enlarged in the inset

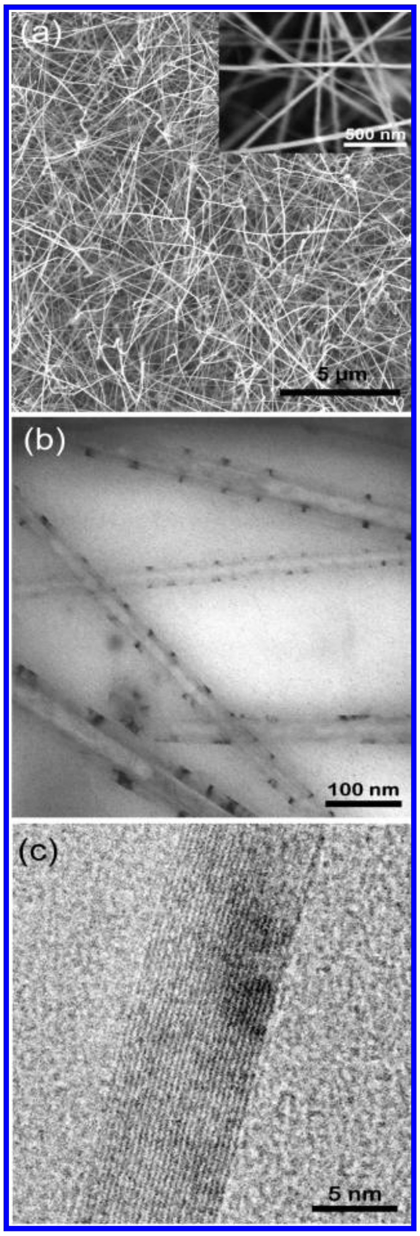

Figure 1. (a) SEM image of MWBNNTs. Inset: Higher magnification SEM image showing straight, slender fibers 15−60 nm in diameter. (b) Low resolution TEM image of MWBNNTs. (c) High resolution TEM image of a MWBNNT wall near a typical dark spot shown in part b.

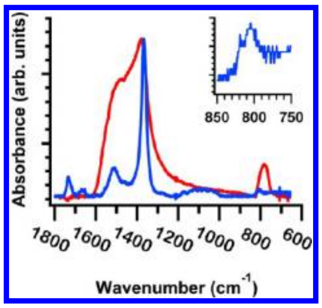

Figure 2. FTIR spectrum of MWBNNTs (blue line). The FTIR spectrum of *h*-BN nanoparticles (red line) is also shown for comparison.

of Figure 2. A shoulder is visible at ~819 cm^{-1} and a peak at ~806 cm^{-1}. These spectral features correspond to the out-of-plane TO and LO A_{2u} modes of *h*-BN.[24,38]

AFM Three-Point Bending. In three-point bending experiments, slender wires can be modeled as an elastic string (pure stretching), a stiff beam (pure bending), or a combination of the two. Heidelberg et al.[39] presented a generalized approximation for these behaviors, in which a force F is applied to the midpoint of the suspended wire and the wire ends are assumed to be clamped:

$$F_{\mathrm{center}} = \frac{192 E_{\mathrm{B}} I}{L^3} \delta_{\mathrm{center}} \left(1 + \frac{A}{24 I} \delta_{\mathrm{center}}{}^2\right) \tag{1}$$

In the above expression, δ is the deflection of the wire, E_{B} is the bending modulus, A is the cross-sectional area of the wire, and I is the second moment of area. At small displacements, the wire undergoes pure bending which is described by the first linear term. At large displacements, axial tensile stresses are induced as the wire stretches which are described by the cubic second term ($F \propto \delta^3$). In this study, only pure bending is considered because the experiments are conducted within the small deflection regime, in which the maximum deflection does not exceed the radius of the wire.

To model the MWBNNTs in this study as stiff beams undergoing pure bending, Euler−Bernoulli beam theory was employed. It should be noted that this theory assumes a homogeneous isotropic material, which is not the case for multiwall nanotubes. Nevertheless, simulations indicate that this approximation offers an adequate description of nanotube bending mechanics prior to buckling.[40] As a result, this approach has been widely used in AFM bending experiments on nanowires and nanotubes.[26−29,31] Unique solutions to the beam equation depend on the boundary conditions of the beam ends, which can be considered to be clamped (no deflection or slope at beam end) or simply supported (no deflection or bending moment at beam end). Beam schematics are presented in Figure 3, which summarize the three models considered in this work: simply supported beam model (a, SSBM), double clamped beam model (b, DCBM), and mixed support beam model (c, MSBM).[41]

The corresponding equations are as follows:

SSBM:

$$F = \frac{3 L E_{\mathrm{B}} I}{a^2 b^2} \delta \tag{2}$$

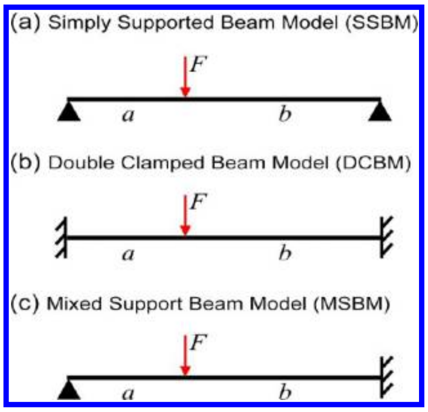

Figure 3. Beam schematics describing beam bending boundary conditions.

DCBM:

$$F = \frac{3L^3E_BI}{a^3b^3}\delta \tag{3}$$

MSBM:

$$F = \frac{12L^3E_BI}{a^2b^3(3L + a)}\delta \tag{4}$$

In these equations, L is the suspended length of the beam and a and b are the suspended lengths on both sides of the applied force F, where $a + b = L$. I, the second moment of area, is taken to be $I = \pi D^4/64$ which is defined for a solid cylindrical wire with a circular cross section, where D is the diameter. Hence, in this approximation of the multiwall nanotube beam, only the outer diameter is taken into account and not the inner diameter. In order to determine the appropriate boundary conditions for each tube, the AFM tip is used to apply a force at different positions along the suspended tube, not just at the midpoint. Therefore, AFM force curves (plots of F versus the tip−sample separation (=beam deflection, δ)) are collected at multiple locations along the tube. The linear slope of a force curve directly yields the effective tube stiffness, $k_{\mathrm{eff}} = F/\delta$. The boundary conditions for the tube are determined by plotting k_{eff} versus the position along the tube (a/L) and performing fits to the various beam models (eqs 2−4). The bending modulus E_B is then determined using the appropriate beam model.

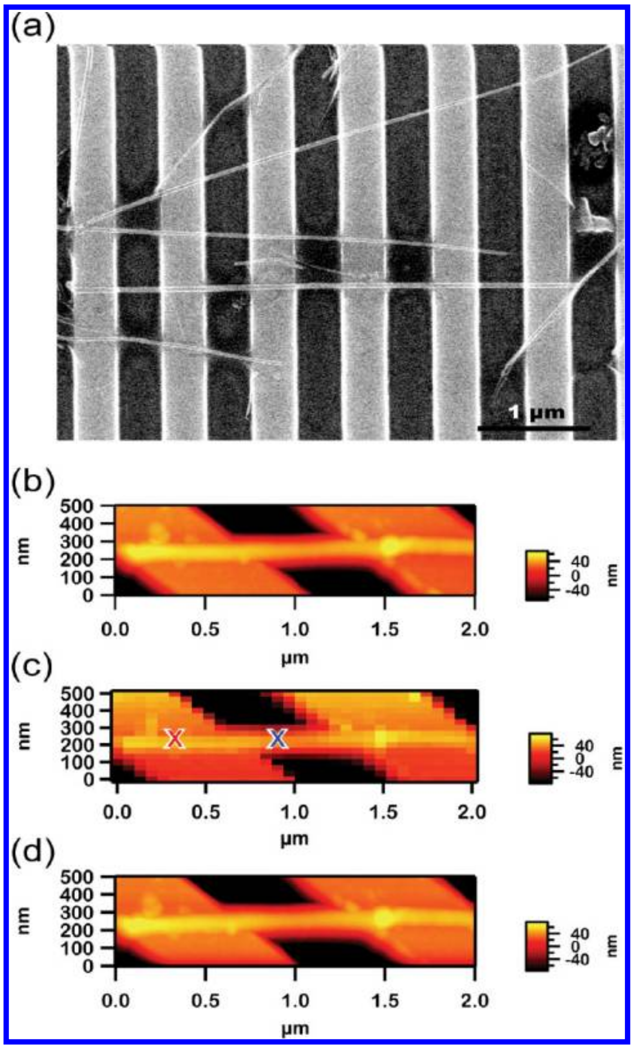

Figure 4. (a) SEM image of MWBNNTs on patterned Si substrate. (b) AFM height image before force mapping was performed. (c) Height map image corresponding to a force map acquired at a deflection trigger of 1 nm. (d) AFM height image after a force map was acquired.

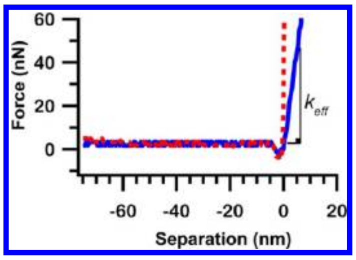

Figure 5. (Red dotted line) Force curve obtained from a point on a tube supported by substrate. (Blue solid line) Force curve obtained from a point on a tube suspended over a trench.

Figure 4 shows SEM (a) and AFM images (b−d) of suspended MWBNNTs on patterned Si trenches (400 nm wide and 200 nm deep). An AFM height image of a typical MWBNNT spanning a trench is shown in Figure 4b. The height image is subsequently divided up into pixels (typically 32 × 16 or 64 × 32) by the AFM software, and force curves are collected at each point (pixel) during the force mapping procedure. The corresponding AFM height map image illustrating the spatial location (x, y) of each of the force measurements is shown in Figure 4c. The height in each pixel is determined from the Z range distance at which the tip first engages the sample during the extend portion of the force curve. Figure 4d shows the AFM height image of the MWBNNT after the force map was performed, and its similarity to Figure 4b indicates that the tube did not shift or deform as a result of the force measurements. Typical force curves collected from different locations on a MWBNNT are shown in Figure 5. The red dotted line corresponds to a force curve obtained from a location where the tube is supported by the Si substrate (red "x" in Figure 4c, illustrative purpose only), while the blue solid line corresponds to a force curve obtained from a position where the tube is suspended over a trench (blue "x" in Figure 4c, illustrative purpose only). The slope of the blue solid line in Figure 5 is equivalent to k_{eff}, as shown.

Plots of the effective tube stiffness (k_{eff}) versus position along the suspended tube (a/L) fitted with eqs 1−3 corresponding to SSBM, DCBM, and MSBM are given in Figure 6. The values of k_{eff} located near the ends $(a/L < 0.2, a/L > 0.8)$ of the suspended tubes were not included in the fits, because of the large error associated with fitting force curves with large slopes (theoretically, at the ends, k_{eff} approaches infinity). Figure 6a shows that SSBM fits the data better than DCBM, signifying that the MWBNNT is an example of a simply supported tube. On the other hand, the data in Figure 6b fits the MSBM model well and is therefore an example of a tube which is fixed on one end (its left side) and simply supported on the opposite end (its right side). Despite the fact that all of the tubes examined were on the same sample, various support conditions were observed which demonstrate the importance of determining the boundary conditions for each individual tube.

Elastic Properties. The bending moduli E_B determined for 20 tubes with diameters ranging from 18 to 55 nm are shown in Figure 7. E_B ranged from 100 ± 20 to 1800 ± 300 GPa, with an average of 760 ± 30 GPa. The error in E_B was determined via error propagation, using an error of 10% for the tube outer

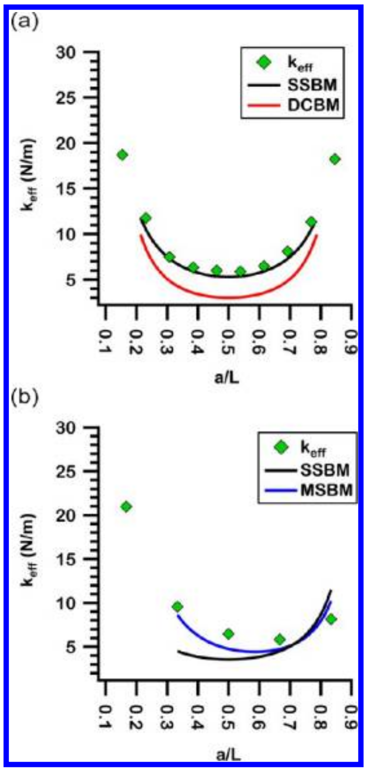

Figure 6. Tube effective stiffness (k_{eff}) vs position along suspended tube (a/L). (a) A simply supported tube. (b) A mixed support tube, with the left side fixed and the right side simply supported.

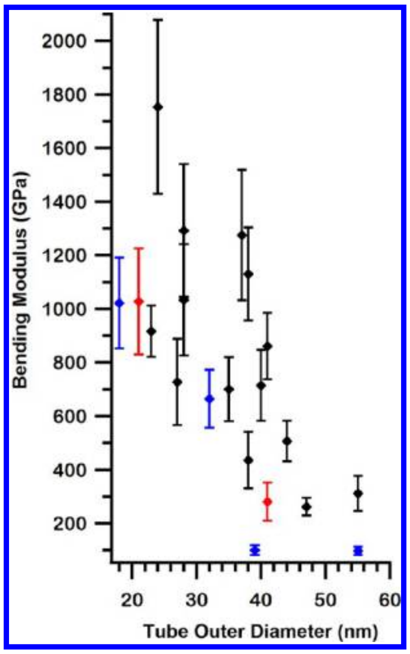

Figure 7. Bending modulus vs tube outer diameter. The beam model used for calculating E_B is denoted by black (SSBM), blue (MSBM), and red (DCBM).

diameter D, half the lateral pixel width in the force map for the tube length L and lengths on each side of the loading position (a, b), and an error of 20% for the effective spring constant of the tube k_{eff}.

It is worth noting that there is the possibility that the calculated bending moduli may be underestimated due to inaccurate assumptions about the cross-sectional geometry. The nanotubes were approximated to be solid wires, with a solid circular cross section. This model was chosen because it was not possible for us to determine the inner diameter of the nanotubes we probed with AFM, given that we deposited the tubes on a substrate that is not amenable to TEM analysis. A more accurate model would be a hollow cylinder, with an inner diameter D_i and an outer diameter D_o, which results in a second moment of area expression of $I = \pi/64(D_o^4 - D_i^4)$. Modeling the tube as a solid wire as opposed to a hollow cylinder underestimates the modulus; however, in the most extreme case (i.e., very large diameter tube with only a few walls), the underestimation is on the order of 30%. On the basis of the range of D_i/D_o ratios observed in TEM data for 24 tubes in the same MWBNNT production batch as the tubes used in the bending experiments (presented in the Supporting Information), the underestimation is closer to 10% for our particular sample.

The Young's modulus of nanotubes and nanowires made of homogeneous isotropic materials such as B and B_4C are typically comparable to the Young's modulus of the bulk material.[42−44] However, for highly anisotropic nanomaterials including CNTs and BNNTs, the Young's modulus should theoretically approach an upper limit defined by the in-plane elastic constant of graphite and *h*-BN, respectively, which exceeds the Young's moduli of the bulk materials by 2 orders of magnitude.[4,45] For *h*-BN single crystals, this constant was measured to be c_{11} = 811 GPa,[46] while, for single crystal graphite, c_{11} = 1109 GPa.[4,45] These measurements correlate well with various theoretical calculations.[47−49] This limit is expected to apply to MWBNNTs as well, because the modulus depends mainly on intrawall bonds. Simulations suggest that the Young's modulus of a MWCNT is slightly higher than that of a SWCNT, for the same outer diameter, due to the effect of interwall van der Waals forces in MWCNTs.[50]

From the plot of E_B versus tube outer diameter shown in Figure 7, it is evident that there is a decreasing trend for the bending modulus with increasing tube diameter. The average E_B of the MWBNNTs studied in the present investigation matches the c_{11} elastic constant of *h*-BN quite closely; however, the origin of the wide range of bending moduli and the diameter dependence requires further analysis.

In experimental studies of multiwall nanotubes, a wide range of modulus values has been measured. For MWCNTs, Treacy et al.[21] were first to show that CNTs have Young's moduli in the TPa range, using a thermal excitation method. They found that arc-discharge MWCNTs with outer diameters ranging from 5.4 to 24.8 nm had Young's moduli of 0.4 to 4.15 TPa. A number of other studies have also produced Young's moduli in the TPa range, for arc-discharge MWCNTs.[26,27,51,52] Within these studies, despite the focus on the ~1 TPa measurements as validation of the superior mechanical properties of CNTs, there are many instances of tubes with lower moduli, on the order of tens to hundreds of GPa. In the work of Salvetat et al.,[27] catalytic CVD MWCNTs were also studied and found to have an average modulus of 27 GPa, which is dramatically lower than the average modulus of 810 GPa measured for arc-discharge MWCNTs. Additional studies also observe lower moduli for catalytic CVD and pyrolytic MWCNTs, in certain cases as low as tens of GPa.[28,53−55] Typically, catalytic CVD and pyrolysis synthesis methods produce tubes with defective structures compared with the highly crystalline tubes synthesized by arc-discharge. While point defects do not affect the modulus by more than a few percent,[56] extended defects can cause the modulus to drop by as much as 2 orders of magnitude.[27,54]

In some studies, within sample sets of nanotubes produced under the same conditions, the modulus is observed to drop with increasing tube diameter. This diameter dependence can be attributed to three possibilities, namely, the probing of an elastic rippling mode in bending experiments,[52] the presence of defects,[28,55] or shear effects. Because of the highly anisotropic nature of the BNNTs, we do not consider surface stress effects which are known to give rise to diameter dependent moduli in relatively isotropic nanowires and nanotubes.[57] Due to the linearity of the force curves obtained in the present study, it is unlikely that rippling modes are the cause of the low moduli measurements observed for larger tubes. Although it was not rare to acquire force curves which exhibited kinks, potentially due to tube buckling or tip slipping events, fits were only made to the initial linear portion of the force curves (for deflections less than 10 nm) after contact. In terms of defects, the low resolution TEM image (Figure 1b) shows long, straight nanotubes with uniform diameters. The high resolution TEM image (Figure 1c) shows that the dark spots present in the tube walls in Figure 1b are crystalline. The MWBNNTs do not appear to exhibit the type of pronounced structural defects that were found to affect the modulus of catalytic or pyrolytic MWCNTs, as discussed above. In beam bending experiments, shear must always be considered for short, stocky beams—those which have a length-to-diameter ratio of $L/D < 10$. The length-to-diameter ratio L/D was measured to be greater than 10 for all tubes in this study, which indicates that, if shear effects are present, they are not a result of the experimental geometry. Rather, they can be an indication of a material's anisotropy.[28,58]

If shear effects are present, then the bending modulus is not equivalent to the Young's modulus. In order to determine whether the Young's modulus of the MWBNNTs is diameter dependent, the contribution of shear deflection to the total deflection in the bending experiment must be quantified. This approach follows Salvetat and co-workers' bending and shear analysis of single-wall CNT ropes.[59]

The bending modulus is related to the Young's modulus E_Y and the shear modulus G using the following relationship, determined by Timoshenko beam theory:[28,59−61]

$$\frac{1}{E_B} = \frac{1}{E_Y} + \gamma\frac{f_s}{G}\left(\frac{D^2}{L^2}\right) \tag{5}$$

In this expression, f_s is a shape factor which has a value of 10/9 for a cylindrical beam and γ is a shear term coefficient with values of 3, 1.715, and 0.75 for DCBM, MSBM, and SSBM, respectively. The Timoshenko beam theory converges to the Euler−Bernoulli beam theory when the beam is rigid in shear ($G \to \infty$). In this case, the bending modulus is equal to the Young modulus and is not diameter dependent (which is not the case here). E_Y and G in our case can be estimated by plotting $1/E_B$ against (D^2/L^2), as shown in Figure 8. A linear fit weighted by the error in $1/E_B$ was obtained for a trimmed data set of 16 tubes. The shear coefficient was taken as $\gamma = 1.152$, determined by the number of tubes exhibiting each type of boundary condition (16 tubes total = 12 simply supported tubes + 2 mixed support tubes + 2 doubly clamped tubes). E_Y and G were determined to be 1800 ± 300 and 7 ± 1 GPa, respectively. The expected shear modulus for a MWBNNT should be on the order of several hundred GPa, based on the calculations for MWCNTs[50,62] which find that $G_{\mathrm{MWCNT}} \sim 500$ GPa. This value is on the order of the intralayer shear modulus. However, the value of G that we determined for MWBNNTs is much lower than this, and is close to the value of the c_{44} elastic constant of h-BN, $c_{44} = 7.7 \pm 5$, measured by Bosak et al.[46] This elastic constant is equivalent to the interlayer shear modulus of h-BN, and describes the shear between basal planes. In the case of the MWBNNT structure, this corresponds to shearing between tube walls, which can only occur if there are discontinuities due to the presence of extended defects within the tube walls.

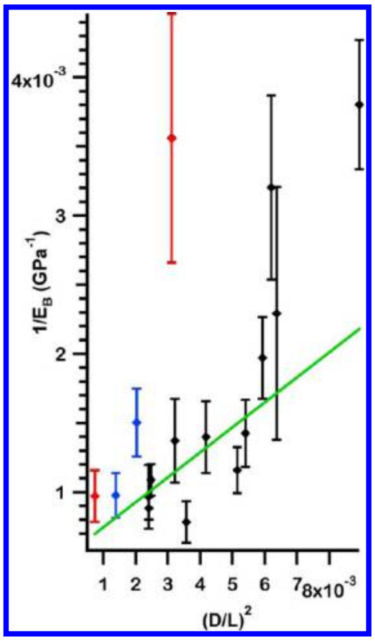

Figure 8. Determination of the Young's modulus and shear modulus *via* a fit to a plot of $1/E_B$ vs $(D/L)^2$. The beam model used for calculating $1/E_B$ is denoted by black (SSBM), blue (MSBM), and red (DCBM). The equation used for the fit is $1/E_B = 1/E_Y + 1.139 f_s/G\,(D^2/L^2)$.

Although no extensive defects are apparent from the TEM characterization of the MWBNNTs, as discussed above, the dark spots within the tube walls in the low resolution TEM image (Figure 1b) and their somewhat regular pattern within a given tube warrant additional consideration. A detailed electron diffraction study by Celik-Aktas et al.[63] determined that the dark spots can be attributed to a helical nanotube structure in which the tube is comprised of two or more helices (each comprised of multiple walls) which wrap to form the entire nanotube. In this structure, the dark spots correspond to a strongly diffracting helix, which is locally highly crystalline. The highly crystalline regions are joined together by line defects which result in a faceted helix. The lighter regions of the tube wall form the other helix, which possesses the conventional nested coaxial cylindrical structure expected for multiwall nanotubes. On the basis of this multihelix nanotube structure, it is conceivable that the line defects within the faceted helix as well as the interface between faceted and cylindrical helices make interwall shearing a possibility. Therefore, as our analysis of the bending data suggests, shear cannot be ignored in the calculation of the elastic modulus, and shear effects arise from nanotube anisotropy ($G \ll E_Y$) and the presence of defects within the nanotubes, and not from the experimental geometry.

Our finding that the shear modulus of MWBNNTs is orders of magnitude smaller than the Young's modulus indicates that the existing theoretical models are not sufficient in predicting the mechanical properties of such extremely anisotropic structures, particularly when structural defects are present.[50] Experiments performed on MWCNTs support this assertion. Guhados et al.[64] determined that $E_Y = 350 \pm 110$ GPa and $G = 1.4 \pm 0.3$ GPa for 13 MWCNTs grown by a CVD method, while Wei et al.[65] found that E_Y ranged from 300 to 900 GPa, while G ranged from 30 to 800 MPa, for a sample of eight tubes. Both studies attribute the low shear modulus to defects in the structure of the nanotubes. There are several possible benefits of having a low shear modulus: (1) Taking advantage of its high melting temperature, the shear modulus of MWBNNTs cast within metals or ceramics would enable damping of vibrations. This could result in quieter, more durable materials.[66−68] (2) Local distortions allowed due to the low shear modulus could enable MWBNNTs to adapt to local structure variations while maintaining rigidity on long length scales (longitudinal distortions), imparting toughness to otherwise brittle composite materials.[51] (3) The mutual compensation of shear modulus and Young's modulus, whereby tubes of different diameters have similar bending stiffness, could allow for lower purity BNNT materials in BNNT coated interfaces for release applications.[69,70] (4) With a shear modulus on the order of the value for *h*-BN, MWBNNTs can be used as a high-temperature solid lubricant additive in industrially relevant composites.[71] The nanotube structures would have the added advantages of enabling more efficient heat transport on longitudinal length scales,[6] and increasing the wear resistance of the composite due to reinforcement of the matrix.[72]

■ CONCLUSIONS

The bending modulus of individual multiwall boron nitride nanotubes (MWBNNTs) was measured *via* AFM bending experiments. Boundary conditions for the beam bending model were determined by using a force mapping technique. MWBNNTs were found to have excellent mechanical properties, with an average bending modulus of 760 ± 30 GPa, which is consistent with the theoretically predicted value for BNNTs. Shear effects were found to be non-negligible, and the Young's modulus and shear modulus were determined to be 1800 ± 300 and 7 ± 1 GPa, respectively. The experimental geometry and the dimensions of the nanotubes were not major contributors to the shear effects; rather, it is likely that interwall shearing occurred between crystalline and faceted cylindrical helices in these MWBNNTs.

■ ASSOCIATED CONTENT

Ⓢ Supporting Information

Details of spring constant determination, error analysis, and force mapping. An analysis of the inner and outer tube diameters based on TEM measurements is also presented. This material is available free of charge via the Internet at http://pubs.acs.org.

■ AUTHOR INFORMATION

Corresponding Author

*E-mail: gwalker@chem.utoronto.ca.

Present Address

‖Department of Mechanical Engineering and Materials Science, Rice University, Houston, Texas 77005.

Author Contributions

The manuscript was written through contributions of all authors. All authors have given approval to the final version of the manuscript.

Notes

The authors declare no competing financial interest.

■ ACKNOWLEDGMENTS

Financial support for this work is provided by the Natural Science and Engineering Research Council of Canada (NSERC). The authors wish to thank N. Coombs of the Centre for Nanostructure Imaging at the University of Toronto for the high resolution TEM images. Y.K.Y. acknowledges U.S. Department of Energy, the Office of Basic Energy Sciences (Grant No. DE-FG02-06ER46294) and National Science Foundation (CAREER Award No. 0447555) for supporting the efforts on the study of boron nitride nanotubes.

■ ABBREVIATIONS

AFM, atomic force microscope/microscopy; DCBM, double clamped beam model; FTIR, Fourier transform infrared; MSBM, mixed support beam model; MWBNNT, multiwall boron nitride nanotube; SEM, scanning electron microscope/microscopy; SSBM, simply supported beam model; TEM, transmission electron microscope/microscopy

■ REFERENCES

(1) Rubio, A.; Corkill, J. L.; Cohen, M. L. *Phys. Rev. B* **1994**, *49*, 5081−5084.
(2) Blase, X.; et al. *Europhys. Lett.* **1994**, *28*, 335−340.
(3) Chopra, N. G.; Luyken, R. J.; Cherrey, K.; Crespi, V. H.; Cohen, M. L.; Louie, S. G.; Zettl, A. *Science* **1995**, *269*, 966−967.
(4) Hernandez, E.; Goze, C.; Bernier, P.; Rubio, A. *Appl. Phys. A: Mater. Sci. Process.* **1999**, *68*, 287−292.
(5) Verma, V.; Jindal, V. K.; Dharamvir, K. *Nanotechnology* **2007**, *18*, 435711−435716.
(6) Bando, Y.; Golberg, D.; Tang, C.; Zhang, J.; Ding, X.; Fan, S.; Liu, C. *J. Phys. Chem. B* **2006**, *110*, 10354−10357.
(7) Chen, Y.; Zou, J.; Campbell, S. J.; Caer, G. L. *Appl. Phys. Lett.* **2004**, *84*, 2430−2432.
(8) Zhi, C. Y.; Bando, Y.; Wang, W. L. L.; Tang, C. C. C.; Kuwahara, H.; Golberg, D. *J. Nanomater.* **2008**, 642036−642035.
(9) Ravichandran, J.; Manoj, A. G.; Liu, J.; Manna, I.; Carroll, D. L. *Nanotechnology* **2008**, *19*, 085712−085715.
(10) Bando, Y.; Golberg, D.; Tang, C.; Terao, T.; Zhi, C. Y. *Pure Appl. Chem.* **2010**, *82*, 2175−2183.
(11) Choi, S. R.; Bansal, N. P.; Garg, A. *Mater. Sci. Eng., A* **2007**, *460−461*, 509−515.
(12) Lahiri, D.; Singh, V.; Benaduce, A. P.; Seal, S.; Kos, L.; Agarwal, A. *J. Mech. Behav. Biomed. Mater.* **2011**, *4*, 44−56.
(13) Ma, R. Z.; Bando, Y.; Zhu, H. W.; Sato, T.; Xu, C. L.; Wu, D. H. *J. Am. Chem. Soc.* **2002**, *124*, 7672−7673.
(14) Reddy, A. L. M.; Tanur, A. E.; Walker, G. C. *Int. J. Hydrogen Energy* **2010**, *35*, 4138−4143.
(15) Ciofani, G.; Raffa, V.; Yu, J.; Chen, Y.; Obata, Y.; Takeoka, S.; Menciassi, A.; Cuschieri, A. *Curr. Nanosci.* **2009**, *5*, 33−38.
(16) Jaffrennou, P.; Barjon, J.; Lauret, J. S.; Maguer, A.; Golberg, D.; Attal-Tretout, B.; Ducastelle, F.; Loiseau, A. *Phys. Status Solidi B* **2007**, *244*, 4147−4151.
(17) Li, L. H.; Chen, Y.; Lin, M. Y.; Glushenkov, A. M.; Cheng, B. M.; Yu, J. *Appl. Phys. Lett.* **2010**, *97*, 141104−141103.

(18) Chowdhury, R.; Adhikari, S. *IEEE Trans. Nanotechnol.* **2011**, *10*, 659−667.
(19) Pampaloni, F.; Florin, E.-L. *Trends Biotechnol.* **2008**, *26*, 302−310.
(20) Chopra, N. G.; Zettl, A. *Solid State Commun.* **1998**, *105*, 297−300.
(21) Treacy, M. M. J.; Ebbesen, T. W.; Gibson, J. M. *Nature* **1996**, *381*, 678−680.
(22) Suryavanshi, A. P.; Yu, M. F.; Wen, J. G.; Tang, C. C.; Bando, Y. *Appl. Phys. Lett.* **2004**, *84*, 2527−2529.
(23) Golberg, D.; Costa, P. M. F. J.; Lourie, O.; Mitome, M.; Bai, X.; Kurashima, K.; Zhi, C.; Tang, C.; Bando, Y. *Nano Lett.* **2007**, *7*, 2146−2151.
(24) Ghassemi, H. M.; Lee, C. H.; Yap, Y. K.; Yassar, R. S. *J. Appl. Phys.* **2010**, *108*, 024314−024314.
(25) Arenal, R.; Golberg, D.; Wang, M.-S.; Xu, Z.; Loiseau, A. *Nanotechnology* **2011**, *22*, 265704−265706.
(26) Salvetat, J. P.; Bonard, J. M.; Thomson, N. H.; Kulik, A. J.; Forro, L.; Benoit, W.; Zuppiroli, L. *Appl. Phys. A: Mater. Sci. Process.* **1999**, *69*, 255−260.
(27) Salvetat, J. P.; Kulik, A. J.; Bonard, J. M.; Briggs, G. A. D.; Stockli, T.; Metenier, K.; Bonnamy, S.; Beguin, F.; Burnham, N. A.; Forro, L. *Adv. Mater.* **1999**, *11*, 161−165.
(28) Lee, K.; Lukić, B.; Magrez, A.; Seo, J. W.; Briggs, G. A. D.; Kulik, A. J.; Forró, L. *Nano Lett.* **2007**, *7*, 1598−1602.
(29) Ni, H.; Li, X. D.; Gao, H. S. *Appl. Phys. Lett.* **2006**, *88*, 043108−043103.
(30) Wen, B. M.; Sader, J. E.; Boland, J. J. *Phys. Rev. Lett.* **2008**, *101*, 175502−175504.
(31) Shin, M. K.; Kim, S. I.; Kim, S. J.; Kim, S. K.; Lee, H.; Spinks, G. M. *Appl. Phys. Lett.* **2006**, *89*, 231929−231923.
(32) Shanmugham, S.; Jeong, J.; Alkhateeb, A.; Aston, D. E. *Langmuir* **2005**, *21*, 10214−10218.
(33) Chen, Y.; Dorgan, B. L.; McIlroy, D. N.; Aston, D. E. *J. Appl. Phys.* **2006**, *100*, 104301−104307.
(34) Kluge, D.; Abraham, F.; Schmidt, S.; Schmidt, H.-W.; Fery, A. *Langmuir* **2010**, *26*, 3020−3023.
(35) Gangadean, D.; David, N. M.; Brian, E. F.; Aston, D. E. *Nanotechnology* **2010**, *21*, 225704.
(36) Lee, C. H.; Wang, J. S.; Kayatsha, V. K.; Huang, J. Y.; Yap, Y. K. *Nanotechnology* **2008**, *19*, 455605−455605.
(37) Hutter, J. L.; Bechhoefer, J. *Rev. Sci. Instrum.* **1993**, *64*, 1868−1873.
(38) Wirtz, L.; Rubio, A. *IEEE Trans. Nanotechnol.* **2003**, *2*, 341−348.
(39) Heidelberg, A.; Ngo, L. T.; Wu, B.; Phillips, M. A.; Sharma, S.; Kamins, T. I.; Sader, J. E.; Boland, J. J. *Nano Lett.* **2006**, *6*, 1101−1106.
(40) Iijima, S.; Brabec, C.; Maiti, A.; Bernholc, J. *J. Chem. Phys.* **1996**, *104*, 2089−2092.
(41) Hsu, T. H. *Structural Engineering and Applied Mechanics Data Handbook*; Gulf Publishing Company: Houston, TX, 1988; Vol. *1*: Beams.
(42) Ding, W.; Calabri, L.; Chen, X.; Kohlhaas, K. M.; Ruoff, R. S. *Compos. Sci. Technol.* **2006**, *66*, 1112−1124.
(43) Lin, C.-H.; Ni, H.; Wang, X.; Chang, M.; Chao, Y. J.; Deka, J. R.; Li, X. *Small* **2010**, *6*, 927−931.
(44) Tao, X.; Dong, L.; Wang, X.; Zhang, W.; Nelson, B. J.; Li, X. *Adv. Mater.* **2010**, *22*, 2055−2059.
(45) Santosh, M.; Maiti, P. K.; Sood, A. K. *J. Nanosci. Nanotechnol.* **2009**, *9*, 5425−5430.
(46) Bosak, A.; Serrano, J.; Krisch, M.; Watanabe, K.; Taniguchi, T.; Kanda, H. *Phys. Rev. B* **2006**, *73*, 041402−041404.
(47) Green, J. F.; Bolland, T. K.; Bolland, J. W. *J. Chem. Phys.* **1976**, *64*, 656−662.
(48) Boettger, J. C. *Phys. Rev. B* **1997**, *55*, 11202−11211.
(49) Ohba, N.; Miwa, K.; Nagasako, N.; Fukumoto, A. *Phys. Rev. B* **2001**, *63*, 115207−115209.
(50) Lu, J. P. *Phys. Rev. Lett.* **1997**, *79*, 1297−1300.
(51) Wong, E. W.; Sheehan, P. E.; Lieber, C. M. *Science* **1997**, *277*, 1971−1975.
(52) Poncharal, P.; Wang, Z. L.; Ugarte, D.; de Heer, W. A. *Science* **1999**, *283*, 1513−1516.
(53) Gaillard, J.; Skove, M.; Rao, A. M. *Appl. Phys. Lett.* **2005**, *86*, 233109−233103.
(54) Gao, R. P.; Wang, Z. L.; Bai, Z. G.; de Heer, W. A.; Dai, L. M.; Gao, M. *Phys. Rev. Lett.* **2000**, *85*, 622−625.
(55) Lukic, B.; Forro, L.; Seo, J. W.; Bacsa, R. R.; Delpeux, S.; Beguin, F.; Bister, G.; Fonseca, A.; Nagy, J. B.; Kis, A.; et al. *Nano Lett.* **2005**, *5*, 2074−2077.
(56) Sammalkorpi, M.; Krasheninnikov, A.; Kuronen, A.; Nordlund, K.; Kaski, K. *Phys. Rev. B* **2004**, *70*, 245416−245418.
(57) Cuenot, S.; Frétigny, C.; Demoustier-Champagne, S.; Nysten, B. *Phys. Rev. B* **2004**, *69*, 165410.
(58) Kaplan-Ashiri, I.; Cohen, S. R.; Apter, N.; Wang, Y.; Seifert, G.; Wagner, H. D.; Tenne, R. *J. Phys. Chem. C* **2007**, *111*, 8432−8436.
(59) Salvetat, J. P.; Briggs, G. A. D.; Bonard, J. M.; Bacsa, R. R.; Kulik, A. J.; Stockli, T.; Burnham, N. A.; Forro, L. *Phys. Rev. Lett.* **1999**, *82*, 944−947.
(60) Kis, A.; Mihailovic, D.; Remskar, M.; Mrzel, A.; Jesih, A.; Piwonski, I.; Kulik, A. J.; Benoit, W.; Forro, L. *Adv. Mater.* **2003**, *15*, 733−736.
(61) Timoshenko, S. *Strength of materials*, 3rd ed.; Van Nostrand: New York, 1955.
(62) Shen, L.; Li, J. *Phys. Rev. B* **2005**, *71*, 035412.
(63) Celik-Aktas, A.; Zuo, J. M.; Stubbins, J. F.; Tang, C. C.; Bando, Y. *Acta Crystallogr., Sect. A* **2005**, *61*, 533−541.
(64) Guhados, G.; Wan, W.; Sun, X.; Hutter, J. L. *J. Appl. Phys.* **2007**, *101*, 033514−033515.
(65) Wei, X.-L.; Liu, Y.; Chen, Q.; Wang, M.-S.; Peng, L.-M. *Adv. Funct. Mater.* **2008**, *18*, 1555−1562.
(66) Sueyoshi, H.; Rochman, N. T.; Kawano, S. *J. Alloys Compd.* **2003**, *355*, 120−125.
(67) Deng, C. F.; Wang, D. Z.; Zhang, X. X.; Ma, Y. X. *Mater. Lett.* **2007**, *61*, 3229−3231.
(68) Balani, K.; Agarwal, A. *J. Appl. Phys.* **2008**, *104*, 063517−063516.
(69) Lipp, A.; Schwetz, K. A.; Hunold, K. *J. Eur. Ceram. Soc.* **1989**, *5*, 3−9.
(70) Haubner, R.; Wilhelm, M.; Weissenbacher, R.; Lux, B. Boron Nitrides - Properties, Synthesis and Applications. In *High Performance Non-Oxide Ceramics II*; Jansen, M., Ed.; Springer Verlag: Berlin, Heidelberg, 2002; pp 1−45.
(71) Chen, W.; Gao, Y.; Chen, C.; Xing, J. *Wear* **2010**, *269*, 241−248.
(72) Zhou, S.-m.; Zhang, X.-b.; Ding, Z.-p.; Min, C.-y.; Xu, G.-l.; Zhu, W.-m. *Composites, Part A* **2007**, *38*, 301−306.

Diameter-Dependent Bending Modulus of Individual Multiwall Boron Nitride Nanotubes

Adrienne E. Tanur[†], *Jiesheng Wang*[‡], *Arava L. M. Reddy*[§], *Daniel N. Lamont*[§], *Yoke Khin Yap*[‡],
Gilbert C. Walker[†§]*

†Department of Chemistry, University of Toronto, Toronto, Ontario M5S 3H6, ‡Department of Physics, Michigan Technological University, Houghton, Michigan 49931-1295, §Department of Chemistry, University of Pittsburgh, Pittsburgh, Pennsylvania 15260

*gwalker@chem.utoronto.ca

Supporting Information

Determination of Spring Constant..........2
Error Analysis..........4
Investigation of Inner and Outer Tube Diameter..........4
Force Mapping Technique..........5

Determination of Spring Constant

The spring constants of the AFM cantilevers used were determined by the thermal method described by Hutter and Bechhoefer.[1] The thermal method is reliable for measuring small (< 1 N/m) spring constant cantilevers (i.e. results in errors of ~5-10%), because their relatively large thermal oscillation amplitude (< 1 Å). The method can have a larger error when applied to stiff (>10 N/m) cantilevers because of their smaller thermal oscillation amplitudes (< 10 pm), which can result in a poor signal-to-noise ratio.[2] In order to demonstrate the applicability of the thermal method to the stiff cantilevers used in this work, we present the details of our spring constant determination method, which is based on the thermal method.

The first step in the process is the determination of the deflection (inverse) optical lever sensitivity, which is achieved by collecting force curves from a clean Si substrate and fitting the contact region. Next, a power spectral density plot is acquired via the thermal tune function within the AFM software (MFP-3D v090909, Asylum Research, CA; Igor Pro v6.12, Wavemetrics, OR). A typical PSD plot obtained from a Si probe (NCH, Nano World, Neuchâtel Switzerland) is shown in Figure 1 below.

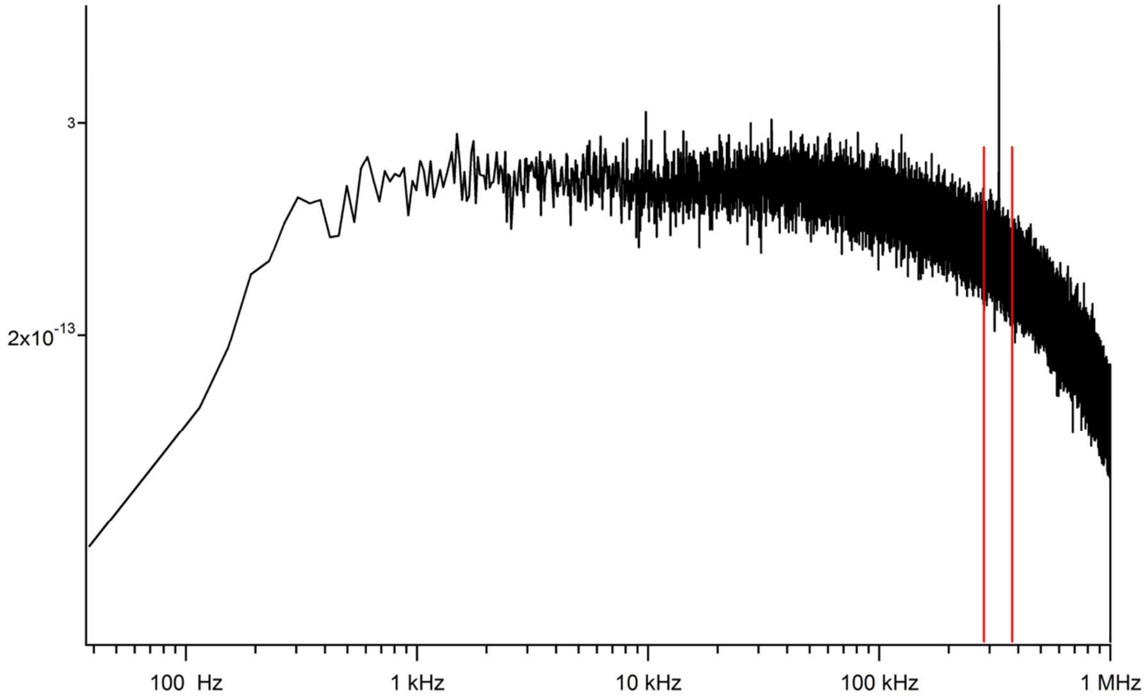

Figure 1: Power spectral density plot for Si cantilever

Figure 2 shows the details of the region containing the first resonance peak (the frequency range is indicated in red in Figure 1). The total PSD is shown in black and the thermal peak fit (damped harmonic oscillator model, Lorentzian lineshape) is shown in blue. The quality factor of this peak is 460, and the signal-to-noise ratio is approximately 16 (intensity of peak:standard deviation of baseline). This signal-to-noise ratio is sufficient for the software to fit the resonance peak without difficulty, and based on the fit parameters the spring constant was calculated by the AFM software using the equations of Hutter and Bechhoefer.[1] The error is estimated to be less than 20%, with the error in the optical lever sensitivity being the major contributor.[3] The spring constants of the cantilevers used in this study were found to range from 33 – 46 N/m. The manufacturer lists the nominal spring constant as 42 N/m, and indicates that a typical range is 21 – 78 N/m.[4] Because the signal-to-noise ratio is high enough to obtain a good fit to the resonance peak, the estimated error of 20% associated with thermal method performed with our instrumentation and software is appropriate for the spring constant error.

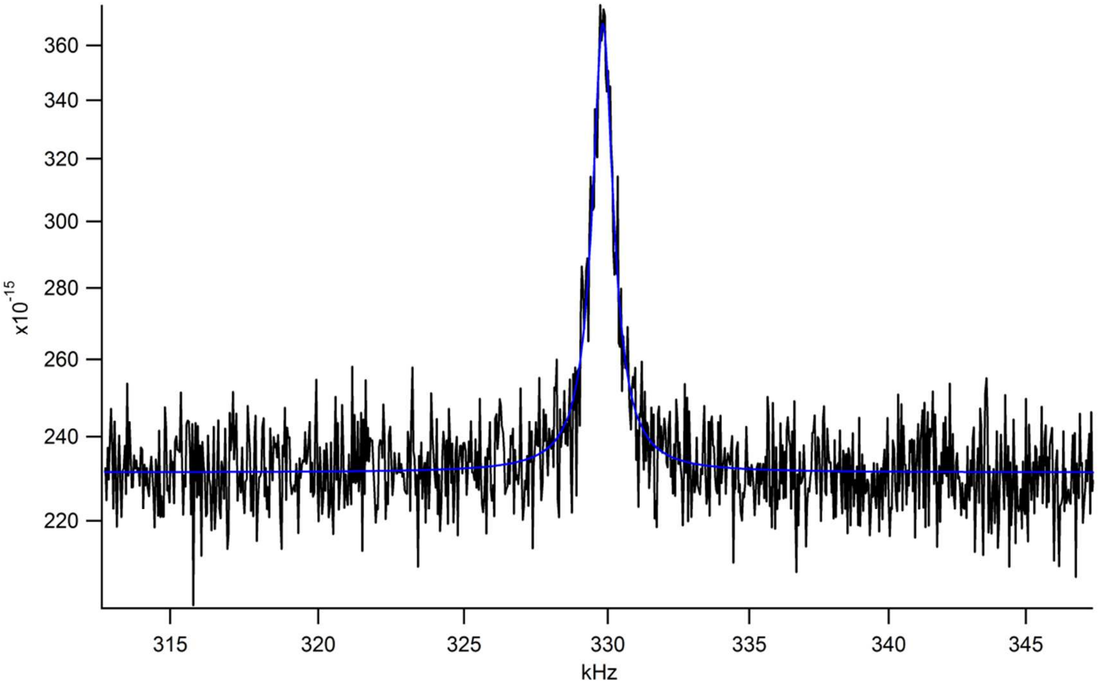

Figure 2: Region of PSD plot containing first resonance peak

References

1. Hutter, J. L.; Bechhoefer, J., Calibration of atomic-force microscope tips. *Rev Sci Instrum* 1993, 64, 1868-1873.
2. Ohler, B., Cantilever spring constant calibration using laser Doppler vibrometry. *Rev Sci Instrum* 2007, 78, 063701-5.
3. Fuierer, R., MFP-3D Procedural Operation 'Manualette' v10. Asylum Research: Santa Barbara, 2008.
4. NanoWorld Type NCH: Non-contact / Tapping™ mode - High resonance frequency. http://www.nanoworld.com/pointprobe-tapping-mode-afm-tip-nch.

Error Analysis

The error for each bending modulus data point was determined via error propagation using an error of 20% in k_{eff}, 10% for the tube outer diameter D, half the lateral pixel width in the force map for the tube length L and lengths on each side of the loading position (a, b), and the standard error in the linear fit for the effective spring constant of the tube k_{eff}.

Investigation of Inner and Outer Tube Diameter

Because one of the limitations of AFM three-point bending experiment is that the inner tube diameter cannot be determined, we have examined our TEM data in further detail in order to better estimate the upper bound of the increase in bending modulus that a hollow tube would give rise to. The inner and outer tube diameters of 24 nanotubes from the same batch of nanotubes used for the AFM measurements are shown in the table below:

Table 1: Tube Diameter Measurements

Tube #	D_{outer} (nm)	D_{inner} (nm)	D_i/D_o
1	64.179	28.358	0.441858
2	33.772	12.665	0.375015
3	22.586	9.079	0.401975
4	64.801	27.763	0.428435
5	20.301	11.367	0.559923
6	27.883	12.308	0.441416
7	45.394	24.841	0.547231
8	45.663	18.158	0.397652
9	27.261	12.006	0.440409
10	30.782	13.089	0.425216
11	35.87	15.256	0.425314
12	47.479	21.657	0.456139
13	67.531	21.739	0.321911
14	27.353	10.184	0.372317
15	35.515	17.519	0.493285
16	47.974	24.234	0.505149
17	67.758	27.888	0.411582
18	32.101	17.622	0.548955
19	56.399	18.293	0.32435
20	46.32	16.362	0.353238
21	35.639	9.289	0.260641
22	28.914	8.979	0.310542
23	31.452	14.917	0.474278
24	17.932	6.044	0.337051

The smallest and largest D_i/D_o ratios are highlighted in red. A smaller ratio corresponds to a more "solid" tube, i.e. thick tube wall, whereas a larger ratio corresponds to a thin-walled tube. The ratio of D_i/D_o ranges from 0.26 to 0.56 for this set of 24 tubes. Using the ratio of 0.56 as the upper bound, the bending moduli calculated in this study are potentially underestimated by ~10%.

Force Mapping Technique

For further description of the force mapping technique and how it can be used for mechanical property mapping, please see the following references:

Sullan, R.M.A. et al. Cholesterol-dependent nanomechanical stability of phase-segregated multicomponent lipid bilayers. *Biophysical Journal* **99** (2010) 507-516.

Ip, S.; Li, J.K.; Walker, G.C. Phase segregation of untethered zwitterionic model lipid bilayers observed on mercaptoundecanoic-acid modified gold by AFM imaging and force mapping. *Langmuir* **26** (2010) 11060-11070.